


Summer 2014

Nickel aluminum shape memory alloys via molecular dynamics

Keith Ryan Morrison
Purdue University

Follow this and additional works at: https://docs.lib.purdue.edu/open_access_theses

 Part of the [Atomic, Molecular and Optical Physics Commons](#), [Materials Science and Engineering Commons](#), and the [Nanoscience and Nanotechnology Commons](#)

Recommended Citation

Morrison, Keith Ryan, "Nickel aluminum shape memory alloys via molecular dynamics" (2014). *Open Access Theses*. 657.
https://docs.lib.purdue.edu/open_access_theses/657

This document has been made available through Purdue e-Pubs, a service of the Purdue University Libraries. Please contact epubs@purdue.edu for additional information.

**PURDUE UNIVERSITY
GRADUATE SCHOOL
Thesis/Dissertation Acceptance**

This is to certify that the thesis/dissertation prepared

By Keith Ryan Morrison

Entitled
Nickel Aluminum Shape Memory Alloys via Molecular Dynamics

For the degree of Master of Science in Materials Engineering



Is approved by the final examining committee:

Alejandro Strachan

Eric Kvam

Kevin Trumble

To the best of my knowledge and as understood by the student in the *Thesis/Dissertation Agreement, Publication Delay, and Certification/Disclaimer (Graduate School Form 32)*, this thesis/dissertation adheres to the provisions of Purdue University's "Policy on Integrity in Research" and the use of copyrighted material.

Alejandro Strachan

Approved by Major Professor(s): _____

Approved by: David Bahr

07/28/2014

Head of the Department Graduate Program

Date

NICKEL ALUMINUM SHAPE MEMORY ALLOYS VIA MOLECULAR DYNAMICS

A Thesis

Submitted to the Faculty

of

Purdue University

by

Keith Morrison

In Partial Fulfillment of the

Requirements for the Degree

of

Master of Science in Materials Engineering

August 2014

Purdue University

West Lafayette, Indiana

To my parents

ACKNOWLEDGEMENTS

I would like to specially thank my advisor, Dr. Alejandro Strachan, for all the support and guidance he has given me during my graduate studies at Purdue. He has taught me how to conduct high quality research, as well as how to carry myself in a professional environment. I would also like to thank my committee members, Dr. Eric Kvam and Dr. Kevin Trumble, for their interest in my research and help in achieving this goal.

I am also thankful for my fellow group members, especially Dr. Karthik Guda Vishnu, Dr. Hojin Kim, and Mathew Cherukara, who have given me constructive feedback and assistance with my research.

Last but not least, I would like to give special thanks to my family and friends for their support in my endeavors.

TABLE OF CONTENTS

	Page
LIST OF FIGURES	vi
ABSTRACT	ix
CHAPTER 1. INTRODUCTION.....	1
1.1 Introduction and Motivation	1
1.2 Shape Memory and Superelasticity.....	2
1.3 Role of Nanostructure.....	3
1.4 Shape Memory in Nickel Aluminum Alloys	6
1.5 Thesis Outline	6
CHAPTER 2. ATOMISTIC SIMULATIONS OF MATERIALS	7
2.1 Motivation for Atomistic Simulations.....	7
2.2 Molecular Dynamics	7
2.3 Interatomic Potentials for Metals	8
2.4 The Use of a Thermostat and Barostat in Molecular Dynamics.....	9
2.5 Validation of Force Field.....	10
CHAPTER 3. EFFECT OF SIMULATION SIZE ON MARTENSITIC TRANSFORMATION	12
3.1 Introduction.....	12
3.2 Initial Structures and Methodology	12
3.3 Transformation Under Cooling and Heating	13
3.4 Variability of the Transformation Temperature	15
3.5 Martensite Microstructure	16
CHAPTER 4. EFFECT OF MECHANICAL CONSTRAINTS ON MARTENSITIC TRANSFORMATION.....	19
4.1 Reason for Mechanical Constraints.....	19
4.2 Transformation Temperatures	19
4.3 Martensite Microstructure: Role of Mechanical Constraints.....	21

	Page
CHAPTER 5. MARTENSITIC TRANSFORMATION IN NANOCRYSTALLINE SAMPLES.....	24
5.1 Polycrystalline Structures	24
5.2 Temperature Induced Transformations	24
5.3 Stress Induced Transformation and Superelasticity	29
CHAPTER 6. CONCLUSIONS AND OUTLOOK.....	36
LIST OF REFERENCES	39
PUBLICATION.....	43

LIST OF FIGURES

Figure	Page
Figure 1.1: Picture of an implanted stent designed to maintain the structural integrity of a blood vessel (directly taken from T. Duerig, A. Pelton and D. Stockel, Materials Science and Engineering A 273-275, 149-160 (1999) [1]).....	2
Figure 2.1: Calculated transformation temperature as a function of nickel composition in NiAl disordered SMAs with a periodic size of 20 nm. The top (red) plot shows the transformation temperature from martensite to austenite upon heating. The bottom (blue) plot shows the transformation temperature from austenite to martensite upon cooling.....	10
Figure 2.2: Martensite transformation temperature as a function of Ni content for Ni-rich NiAl samples from both MD and experiments (directly taken from Guda Vishnu, K. and Strachan, A. Journal of Applied Physics 2013;113:103503) [36].	11
Figure 3.1: Lattice parameters as a function of temperature during cooling and heating of a $L = 20$ nm $\text{Ni}_{63}\text{Al}_{37}$ disordered SMA. The transformation to martensite upon cooling occurs at approximately 150K. The subsequent transformation back to austenite upon heating occurs at approximately 1300K.	14
Figure 3.2: Transformation temperature as a function of system size for $\text{Ni}_{63}\text{Al}_{37}$ disordered SMAs. A slight transformation temperature increase is observed as system size is decreased.	15
Figure 3.3: The relative fluctuation as a function of system size for $\text{Ni}_{63}\text{Al}_{37}$ disordered SMAs. Relative fluctuation is defined as the ratio of the standard deviation to the mean. The transformation to martensite shows greatly increased variability as system size is reduced.	16

Figure	Page
Figure 3.4: Atomistic snapshots from Ovito that illustrate the temporal evolution of the microstructure during the martensitic transformation of $\text{Ni}_{63}\text{Al}_{37}$ disordered SMAs. Red atoms signify martensite (HCP-like), blue atoms represent austenite (BCC-like), and green atoms show stacking faults (FCC-like). The 20 nm structure (top) results in a single domain of martensite upon cooling. The 40 nm structure (bottom) transforms and maintains a two-domain microstructure of martensite upon cooling.	18
Figure 4.1: The transformation temperatures as a function of system size for $\text{Ni}_{63}\text{Al}_{37}$ SMAs under mechanical constraints. The austenite transition temperature shows strong size dependence and decreases with decreasing size.....	20
Figure 4.2: The relative fluctuation as a function of system size for $\text{Ni}_{63}\text{Al}_{37}$ disordered SMAs under mechanical constraints. Relative fluctuation is defined as the ratio of the standard deviation to the mean. The variability of the transformation back to austenite now increases with decreasing size, due to the mechanical constraints lowering the austenite transformation temperature for smaller system sizes.	21
Figure 4.3: Atomistic snapshots from Ovito that compare the martensitic microstructure between the constrained and unconstrained systems. The only unconstrained system that resulted in a multi-domain structure is for $L = 40$ nm. The constrained systems formed a multi-domain structure for periodic cell sizes as small as $L = 7$ nm.....	22
Figure 5.1: Percent martensite transformation vs. grain size for $\text{Ni}_{63}\text{Al}_{37}$ disordered SMAs after cooling to 1K at 0.5 K/ps. Percentage transformation is determined by the summed percentage of HCP-like and FCC-like atoms, where grain boundary atoms are not considered in the total.....	26
Figure 5.2: Atomistic snapshots of martensite structures after cooling for a range of grain sizes of $\text{Ni}_{63}\text{Al}_{37}$ disordered SMAs. Blue atoms (BCC-like) represent austenite, while red (HCP-like) and green (FCC-like) atoms represent martensite.....	27
Figure 5.3: Percentage martensite as a function of temperature for different grain sizes of polycrystalline $\text{Ni}_{63}\text{Al}_{37}$ disordered SMAs.....	29

Figure	Page
Figure 5.4: Compilation of stress vs. strain curves for a range of grain sizes of $\text{Ni}_{63}\text{Al}_{37}$ disordered SMAs. The samples were strained uniaxially up to 10%. At 4% and 10% strain, the samples were unloaded and relaxed.	31
Figure 5.5: Atomistic snapshots of a polycrystalline $\text{Ni}_{63}\text{Al}_{37}$ disordered SMA with a grain size of 3.5 nm. Left-to-right illustrates the microstructure from (1) equilibrated, (2) strained to 10%, and (3) relaxed after 10% strain. Blue atoms are BCC-like, red atoms are HCP-like, and green atoms are FCC-like.	32
Figure 5.6: Percent plastic recovery as a function of grain size for polycrystalline samples of $\text{Ni}_{63}\text{Al}_{37}$ disordered SMAs that were strained to either 4 or 10% and subsequently unloaded and relaxed at room temperature.	34
Figure 5.7: Young's Modulus as a function of grain size for polycrystalline samples of $\text{Ni}_{63}\text{Al}_{37}$ disordered SMAs.	35

ABSTRACT

Morrison, Keith R. M.S.M.S.E., Purdue University, August 2014. Nickel Aluminum Shape Memory Alloys via Molecular Dynamics. Major Professor: Alejandro Strachan.

Shape memory materials are an important class of active materials with a wide range of applications in the aerospace, biomedical, and automobile industries. These materials exhibit the two unique properties of shape memory and superelasticity. Shape memory is the ability to recover its original shape by applying heat after undergoing large deformations. Superelasticity is the ability to undergo large, reversible deformations (up to 10%) that revert back when the load is removed. These special properties originate from a reversible, diffusionless solid-solid phase transformation that occurs between a high temperature austenite phase and a low temperature martensite phase. The development of the martensite microstructure is not well understood; this is especially true in regards to the role of size and mechanical constraints that dominate the properties in nanoscale samples. The goals of this research are to use molecular dynamics (MD) to (1) study the effects of simulation size on the martensite transformation to determine the ultimate limit of miniaturization, (2) to investigate the effects of mechanical constraints on the martensite transformation and resulting microstructure, and (3) to explore the effects of grain size in

polycrystalline shape memory alloys. MD is well suited to study the transformation, as it shares a similar time scale with the extremely fast, diffusionless transformation.

An extensive set of cooling and heating simulations were performed on Ni₆₃Al₃₇ disordered shape memory alloys (SMAs) to determine the effect of system size on the transformation. Simulation cell sizes in the range of 4.2 to 20 nm were studied. We discovered that decreasing system size only resulted in a slight increase of both transformation temperatures. However, the variability of the austenite transformation temperature increased considerably with decreasing simulation cell size, reaching 10% of the mean value for a system size of 10 nm. This variability can impose a fundamental limit on the miniaturization of this class of materials, as the reliability of device performance comes into question. Also, mechanical constraints were applied to force the cell angles to remain 90° in order to emulate the environment of a partially transformed polycrystal where grains are constricted by their neighbors. The mechanical constraints caused the austenite transformation temperature to decrease with decreasing size by up to 50%, and resulted in a two-domain microstructure for system sizes above 4.2 nm in order to accommodate the internal stresses. Finally, large scale MD simulations were done on polycrystalline samples with grain sizes ranging from 2.5 to 20 nm. We found that a critical grain size of 7.5 nm resulted in a minimum in the percent transformation to martensite. Below this critical size, martensite forms at the grain boundaries and the grains are able to rotate via grain boundary sliding to relieve internal stresses. In larger grains, martensite can nucleate and

grow within the grains more easily. A uniaxial strain of up to 10% was applied to investigate the stress induced martensite transformation. Larger grains showed considerable work hardening when strained beyond about 2%. Plastic recovery was also calculated by unloading and relaxing at 4 and 10% strain. Samples strained to 10% were generally able to recover about 20-30% of the plastic strain, while samples strained to 4% showed varying amounts of recovery that peaked at 66% for a grain size of 7.5 nm.

CHAPTER 1. INTRODUCTION

1.1 Introduction and Motivation

Shape memory alloys (SMAs) are a very unique and interesting class of materials with a wide range of potential applications. Current uses include implanted stents to keep arteries open (shown in Figure 1.1) [1], micro-actuators[2], mechanical damping, and noise reduction [3,4]. The most common commercial SMA is NiTi, or Nitinol, largely due to its high tensile strength, biocompatibility, corrosion resistance, and near room temperature transformation temperatures. However, other lesser known SMAs exist, including NiAl.

Despite the interest SMAs have received, the transformation to martensite and the resulting microstructure is not well understood. As devices are made smaller and smaller, a greater understanding of the underlying mechanisms will be needed to predict and control properties. At the nanoscale, properties are dominated by size effects and mechanical constraints that control the microstructural development. Furthermore, sample-to-sample variability and variability in the transformation can cripple the reliability of devices at the nanoscale.

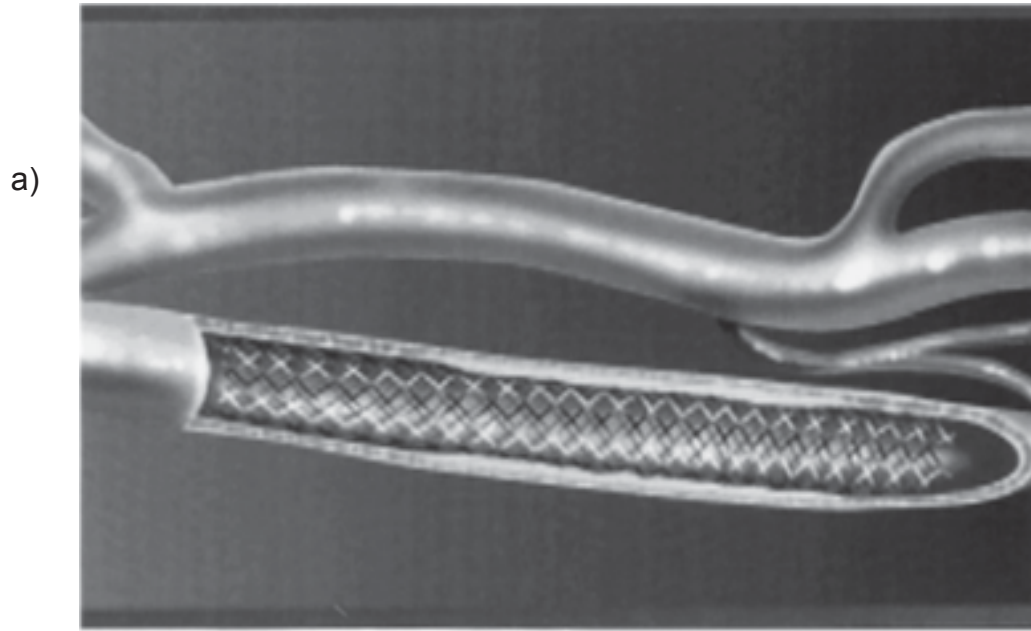


Figure 1.1: Picture of an implanted stent designed to maintain the structural integrity of a blood vessel (directly taken from T. Duerig, A. Pelton and D. Stockel, *Materials Science and Engineering A* 273-275, 149-160 (1999) [1])

1.2 Shape Memory and Superelasticity

The unique properties of SMAs include shape memory and superelasticity. Shape memory is the ability to return to the original shape and configuration after a large deformation, accomplished through heating [4]. Superelasticity is the ability to recover very large strains when the applied stress is removed, which is possible if the SMA is above the transition temperature to austenite [4].

These properties are made possible by the diffusionless, solid-to-solid martensitic phase transformation [5]. The phase transformation involves the switch between a high-symmetry, high-temperature austenite phase (stabilized

by entropy) and a low-temperature martensite phase. The martensitic phase transformation can be induced either thermally or mechanically. The transformation can be described as shear-like. Upon cooling past the critical temperature M_s , the martensite phase begins to form. Due to the martensite having less symmetry than the austenite, multiple variants of the martensite are possible. As a result, multiple domains form in order to accommodate the elastic strain and to try and retain its original shape [5]. It is important to note that the transformation and subsequent plastic deformation does not involve dislocations. Instead, the plastic deformation of the martensite proceeds via domain wall motion, meaning that every atom will retain its nearest neighbors. Therefore, upon transformation back to austenite, the material will have the same atomic configuration, resulting in shape memory [5]. However, this requires that the symmetry groups of austenite and martensite share a common finite symmetry group [6], and that all martensite variants are able to transform to a unique variant of austenite [7]. These requirements ensure that the transformation is reversible at the atomic level.

1.3 Role of Nanostructure

Knowledge is lacking in regards to the development of the martensitic microstructure in nanocrystalline samples. The properties of nanoscale sized samples are dominated by the effects of size and mechanical constraints. Furthermore, NiAl SMAs are disordered alloys, meaning that there is intrinsic atomic variability that will further affect their behavior on the nanoscale. The

martensitic transformation involves expansion along two directions and compression in the third direction. As a result, polycrystalline samples will experience complex internal stress distributions as individual grains will push on one another. Internal stress distributions should therefore affect the transformation temperature or stress locally, resulting in an inhomogeneous martensite microstructure.

Experimental work has begun to show the effects of size on the transformation of polycrystalline SMAs. When stress is applied, favorably oriented grains, which are randomly throughout the sample, will begin to transform first. As the transformation progresses, neighboring grains will constrict the partially transformed grains, resulting in the need for more stress or undercooling to progress the transformation further [8]. On top of the local stress suppressing the transformation, latent heat will also be released, resulting in further suppression of the transformation [8,9]. Experimental work involved examining the martensitic transformation of NiTiCu nanocrystals dispersed within a Ni₅₀Ti₂₅Cu₂₅ matrix. The nanocrystals ranged in size from 10 to 50 nm in diameter. The nanocrystals in the range of 15 to 25 nm showed partial transformation, while nanocrystals over 25 nm in size showed complete transformation to martensite [10]. Other experimental work, done on nanograins of NiTi, revealed that grains under 50 nm in diameter did not transform [11].

Molecular dynamics (MD) simulations have also significantly contributed to our understanding of SMAs and size effects. Solid-solid phase transformations

using MD were pioneered by Rahman and Parrinello. They also warned that simulating small system sizes with periodic boundary conditions was flawed due to size effects [12]. Earlier MD simulations of martensite transformations [13,14] were severely limited due to the small system size. More recent MD work [15,16] showed that the size and shape of Zr and Fe nanowires has a strong effect on the martensite transformation. Others were able to use MD to produce a realistic martensite microstructure of NiAl SMAs in 2-D and describe its formation [17,18].

MD simulations are greatly enhancing our knowledge of martensite nanostructures [19–25], the transformation to martensite [19–29], grain size [23], surface effects [29,30], and mechanical properties of SMAs [26]. In addition, the martensitic transformation of Zr was studied further in recent MD work [19,25]. When Zr is sufficiently cooled, martensite begins to form within the crystal, causing strain in the surrounding material. To alleviate this stress, specific variants of martensite formed. Other MD work looked at SMAs with the B2 to B19 phase transition and found a twinning hierarchy. Domains of martensite would form that contained microtwins, which supplemented the macrotwinning occurring along the bar [25].

In spite of such great results, much is still not well understood in regards to size effects and mechanical constraints on the microstructure and transformation temperature of SMAs. This work focuses on the MD study of NiAl SMAs to enhance our understanding of size effects, mechanical constraints, and sample variability on the martensitic transformation.

1.4 Shape Memory in Nickel Aluminum Alloys

Nickel aluminum exhibits shape memory for a specific range in composition that is Ni-rich. Equiatomic NiAl in the austenite phase has a B2 crystal structure. If more Ni is added, Ni atoms substitute onto the Al sites to create a disordered Ni-rich Alloy. $\text{Ni}_x\text{Al}_{1-x}$ exhibits shape memory for x between 60 and 65% [31]. The austenite phase is B2-based and the martensite phase has a tetragonal $L1_0$ close-packed structure (face-centered tetragonal) [32]. However, the alloy must be quenched to room temperature to avoid the formation of the Ni_5Al_3 phase, which is favorable below 700°C [31].

1.5 Thesis Outline

The remainder of this document is organized as follows: In chapter 2, an introduction to the atomistic simulation of materials has been given. In chapter 3, the effects of simulation size on the martensitic transformation have been discussed. In chapter 4, the effects of mechanical constraints on the martensitic transformation are shown. Chapter 5 describes the martensitic transformation in nanocrystalline samples. Finally, chapter 6 gives conclusions and outlook for future study.

CHAPTER 2. ATOMISTIC SIMULATIONS OF MATERIALS

2.1 Motivation for Atomistic Simulations

While experiments serve a vital role, simulations have several distinct advantages. The martensite transformation is a diffusionless process, making it occur on a time scale best suited for MD simulations [32]. The time and spatial resolution needed to observe the transformation are not achievable in experiments. Also, simulations make it possible to study systems that are extremely hard or even impossible to fabricate. Simulations can therefore be used to expedite development of new materials and systems that may be impractical or too costly to test experimentally. Computational power is rapidly increasing as well, making simulations a much more attractive option pricewise.

2.2 Molecular Dynamics

Molecular dynamics simulations follow the motion of every atom in the system in order to predict the evolution of the system with time. Starting from an initial configuration, MD calculates the trajectory of every atom by numerically solving Newton's classical equations of motion

$$\dot{r}_i = v_i \quad (2.1)$$

$$\dot{v}_i = \frac{F_i}{m_i} \quad (2.2)$$

at each time step, Δt . The size of the time step should be on the order of the fastest vibrations in a solid, resulting in a chosen time step of usually one femtosecond (fs). The forces on atoms are determined by their interaction with other atoms in the system, which is then used to generate positions and velocities for the subsequent time step.

Time integration is carried out using the velocity Verlet method which minimizes the errors associated with time integration. The velocity Verlet method is as follows:

$$P_i(t + \frac{\Delta t}{2}) = P_i(t) + F_i(t) \times \frac{\Delta t}{2}$$

$$r_i(t + \Delta t) = r_i(t) + P_i(t + \frac{\Delta t}{2}) \times \frac{\Delta t}{m_i}$$

Calculate $F_i(t + \Delta t)$ using $r_i(t + \Delta t)$

$$P_i(t + \Delta t) = P_i(t + \frac{\Delta t}{2}) + F_i(t + \Delta t) \times \frac{\Delta t}{2}$$

All MD simulations performed in this study were carried out using a code package developed at Sandia National Laboratories called LAMMPS, which stands for Large scale Atomic/Molecular Massively Parallel Simulator [33].

2.3 Interatomic Potentials for Metals

The interactions between atoms are calculated using an interatomic potential, also known as a force field. The interatomic potential essentially averages the electrons out. The accuracy of properties calculated from MD

simulations is highly dependent on the quality of the interatomic potential used [32].

Interatomic potentials are developed by parameterizing them to experimental data, data from quantum mechanical simulations, or both. The force field used in this work was developed by Farkas et al. [34], and was parameterized by properties including lattice parameters, elastic constants, and stacking fault energies of the B2 NiAl and Ni₅Al₃ phases. The force field was chosen in order to replicate the martensitic phase transformation of NiAl and the strong compositional dependence of the transformation temperature [32,35]. For metals, an embedded atom model (EAM) potential is used to capture many-body effects. The potential energy can be written as:

$$E = \sum_{i,j} V(r_{ij}) + \sum_i F(\bar{\rho}_i) \quad (2.3)$$

$$\bar{\rho}_i = \sum_{i,j} \rho(r_{i,j}) \quad (2.4)$$

where V is the two body pair potential, r_{ij} is the distance between atoms i and j , F is the embedding energy, $\bar{\rho}_i$ is the electron density at atom i due to neighboring atoms within a specified cut-off distance, and ρ is the electron density function.

2.4 The Use of a Thermostat and Barostat in Molecular Dynamics

The simulations carried out in this study were done using an isothermal – isobaric (NPT) ensemble. NPT is a statistical mechanical ensemble in which temperature and pressure are controlled through the use of a thermostat and barostat, respectively. A thermostat is essentially an infinite heat bath that controls the temperature of the system by either dumping energy in or out of the

system. Likewise, a barostat controls the external pressure on the system. This study employed a Nosé-Hoover thermostat and a Parrinello-Rahman barostat [12] with coupling constants of 0.1 and 1.0 picoseconds, respectively.

2.5 Validation of Force Field

MD simulations were performed on a range of compositions of NiAl in order to confirm the Ni compositional dependence of the transformation temperatures. Samples below 61% Ni did not show a phase transformation to martensite. Figure 2.1 shows that both transformation temperatures increased with increasing Ni content for the entire range of 61 to 66% Ni, which is consistent with prior MD simulations using the same force field [32,35].

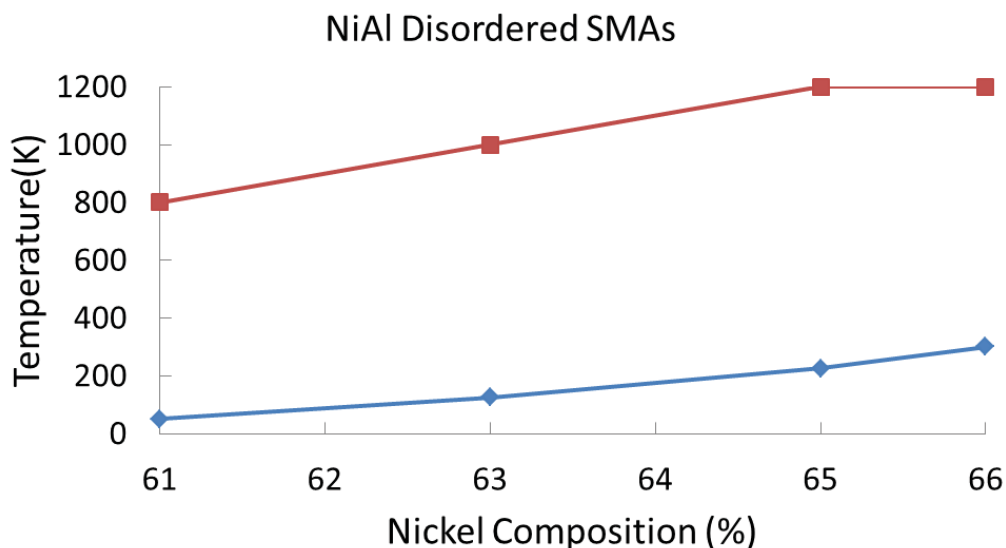


Figure 2.1: Calculated transformation temperature as a function of nickel composition in NiAl disordered SMAs with a periodic size of 20 nm. The top (red) plot shows the transformation temperature from martensite to austenite upon heating. The bottom (blue) plot shows the transformation temperature from austenite to martensite upon cooling.

Figure 2.2 shows the martensite transformation temperature as a function of Ni content for prior MD work using the same force field, as well as experiments of both single crystal and cast samples [35]. The simulations follow the observed trend of increasing martensite transformation temperature with increasing Ni content. Also, the transformation temperatures simulated with MD are lower than experiments, due to having perfect structures without defects as well as very fast cooling rates.

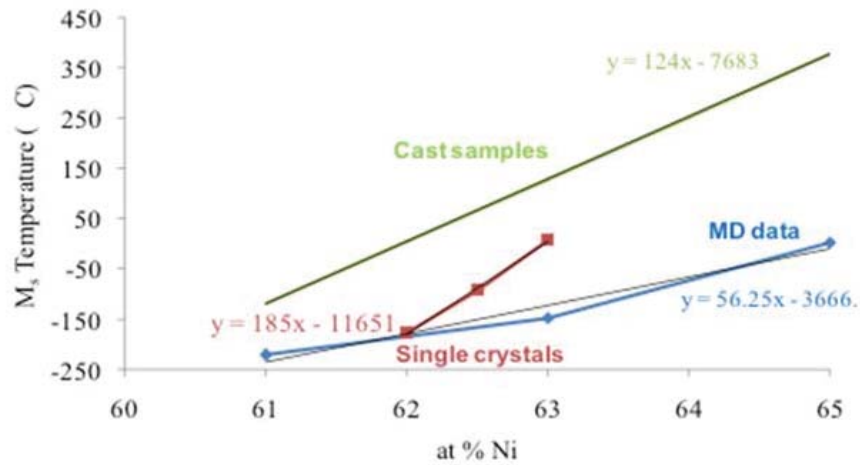


Figure 2.2: Martensite transformation temperature as a function of Ni content for Ni-rich NiAl samples from both MD and experiments (directly taken from Guda Vishnu, K. and Strachan, A. Journal of Applied Physics 2013;113:103503) [36].

CHAPTER 3. EFFECT OF SIMULATION SIZE ON MARTENSITIC TRANSFORMATION

3.1 Introduction

Properties at the nanoscale are dominated by size effects. Decreasing the system size has a profound effect on the martensitic transformation temperature and resulting microstructure. In order to study the size effects of the transformation, a range of periodic cell sizes were used. The sample-to-sample variability is another consideration that becomes increasingly important with smaller sizes. This variability will hurt the reliability of device performance and impose an ultimate limit of miniaturization.

3.2 Initial Structures and Methodology

The initial structures were generated by taking a B2 unit cell of equiatomic NiAl and replicating in all three dimensions to reach the target size. The simulation cell is oriented along the basic $\langle 100 \rangle$ directions. In order to achieve the desired composition necessary for shape memory, Al atoms were randomly replaced with Ni atoms until nickel content reached 63%. Structures in this study ranged in size from approximately 4 nm (6,750 atoms) to 40 nm (5,971,968 atoms). Periodic boundary conditions were applied to all directions, and size refers to the length of the periodic cell. Periodic boundaries allow us to directly study the effects of reducing the number of atoms and maximum allowed size of

microstructural features. Free surfaces would also play a major role in the transformation [37], but that is beyond the scope of this study.

An extensive set of heating and cooling simulations were run using the NPT ensemble, with up to 50 unique structures simulated for each size studied. The simulations used a cooling/heating rate of $\pm 0.5 \text{ K ps}^{-1}$, and a time step of 1 fs. The thermostat and barostat used coupling constants of 0.1 and 1.0 ps, respectively.

3.3 Transformation Under Cooling and Heating

The transformation from the high temperature austenite to the low temperature martensite phase results in the expansion of two $[100]_{\text{bcc}}$ directions and compression along the remaining $[100]_{\text{bcc}}$ direction. Furthermore, a slight cell angle change is observed, changing the structure from cubic to monoclinic ($\alpha = \delta = 90^\circ, \beta \neq 90^\circ$). After the transformation to martensite upon cooling, subsequent heating will eventually transform the sample back to austenite at a higher temperature than the transformation to martensite. This means that there is a hysteresis associated with the transformation, which is consistent with prior MD work [32,38,39].

Figure 3.1 shows lattice parameters as a function of temperature during cooling and subsequent heating for a $\text{Ni}_{63}\text{Al}_{37}$ disordered SMA with 746,496 atoms. The sample starts out as cubic austenite, and upon reaching approximately 150K, the transformation to martensite occurs abruptly and two lattice parameters expand while the third lattice parameter contracts. Upon reheating, the sample doesn't transform into austenite until a temperature of

approximately 1300K is reached, which signifies a significant hysteresis associated with the transformation.

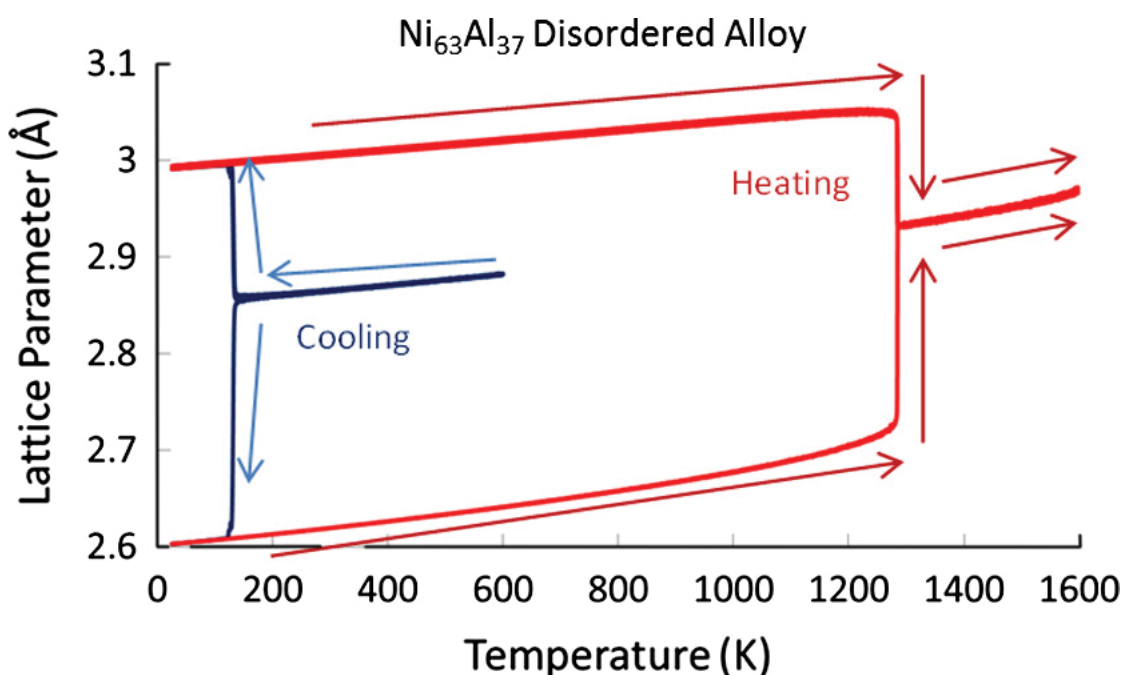


Figure 3.1: Lattice parameters as a function of temperature during cooling and heating of a $L = 20$ nm $\text{Ni}_{63}\text{Al}_{37}$ disordered SMA. The transformation to martensite upon cooling occurs at approximately 150K. The subsequent transformation back to austenite upon heating occurs at approximately 1300K.

Figure 3.2 illustrates the average transformation temperatures for each system size for both the transformation to austenite and martensite. Each system size is represented by at least 10 unique structures. As system size is decreased, both transformation temperatures showed a small increase. This effect indicates that a smaller periodic cell size penalizes the free energy of the entropy-stabilized austenite phase, which could be a result of the reduction in size of allowed phonons.

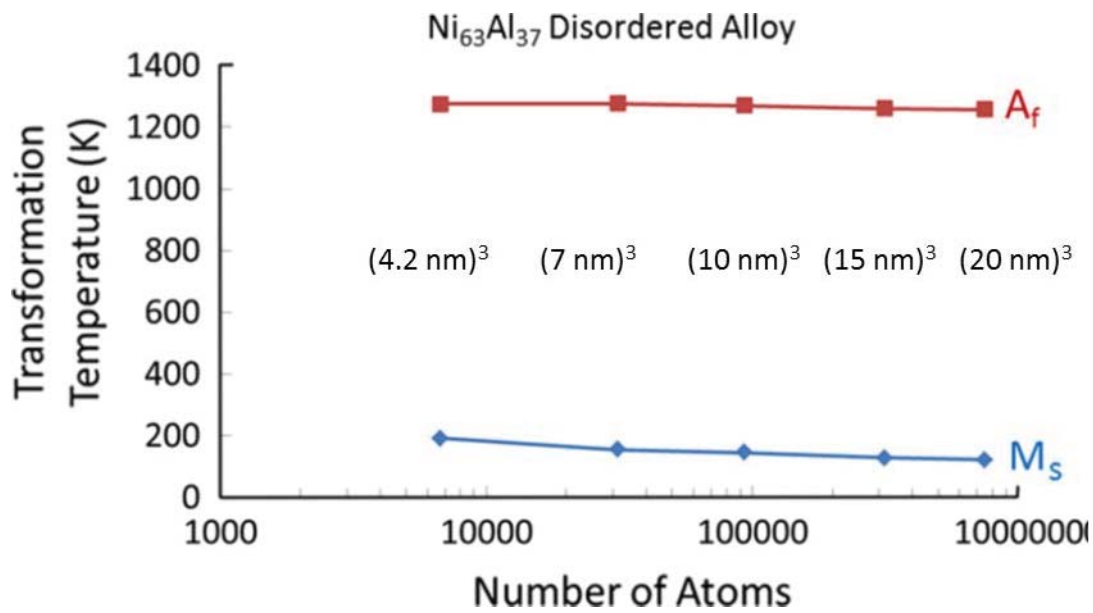


Figure 3.2: Transformation temperature as a function of system size for $\text{Ni}_{63}\text{Al}_{37}$ disordered SMAs. A slight transformation temperature increase is observed as system size is decreased.

3.4 Variability of the Transformation Temperature

Since the samples are generated by randomly replacing Al atoms with Ni atoms, there exists an inherent variability between samples. There is no method in place to prevent clusters of Ni-rich or Ni-poor regions. In large samples, the fluctuations in composition would average out and cancel each other. However, small samples are more likely to see significant changes to the relative energy of the austenite and martensite phases due to these deviations. We anticipate and expect variability of the transformation to increase with decreasing system size.

Figure 3.3 shows the variability of the transformation temperatures as a function of system size. Specifically, the ratio between standard deviation and the mean is shown. The variability in the transformation temperature to martensite increases greatly for reduced system sizes. The variability in the transformation

temperature to martensite is over 10% of the mean for samples up to 10 nm in size. On the other hand, the variability in the transformation to austenite is relatively unaffected by system size. This is most likely due to the very high temperature associated with the phase transition to austenite, where entropy dominates the free energy and minimizes the effects of atomic configurations.

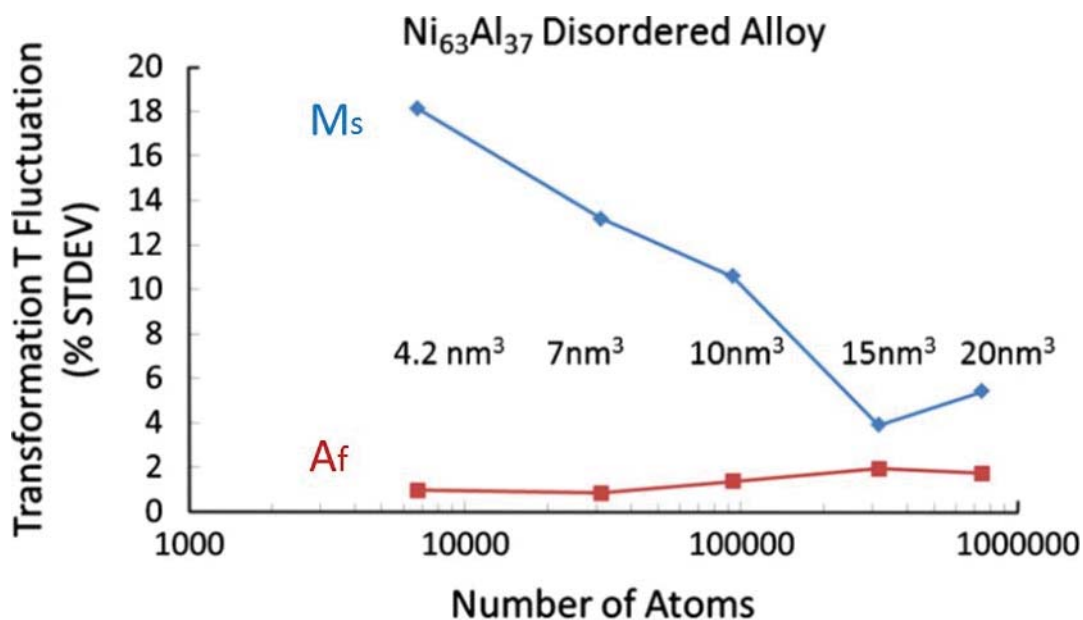


Figure 3.3: The relative fluctuation as a function of system size for Ni₆₃Al₃₇ disordered SMAs. Relative fluctuation is defined as the ratio of the standard deviation to the mean. The transformation to martensite shows greatly increased variability as system size is reduced.

3.5 Martensite Microstructure

In order to characterize the martensite microstructure, a visualization software package, called Ovito [40], was utilized. A dump file from LAMMPS, containing atomic IDs and positions over time, is imported into Ovito for analysis. A common-neighbor analysis is used to analyze the number of nearest neighbors within a specified cut-off radius to determine the local crystal structure. Atoms are

then color-coded based on this analysis. Body-centered cubic (BCC) atoms are colored blue, face-centered cubic (FCC) atoms are colored green, and hexagonal close-packed (HCP) atoms are colored red. The high temperature austenite phase is BCC-like, and appears as blue. The low temperature martensite phase is a combination of HCP-like atoms (red), and FCC-like defects (green).

Figure 3.4 shows atomistic snapshots of the martensite microstructure, as taken from Ovito, during the transformation to martensite. The top sample has a periodic cell length of 20 nm. Multiple variants of martensite are nucleated within the single crystal. Green atoms (FCC) are useful in determining the relative orientations of martensite domains. Both stacking faults and domain walls occur along $\{110\}_{\text{bcc}}$ planes. The only difference between the two domains for this case is the monoclinic angle. These variants of different orientations are able to grow into and consume one another, until only one variant remains. On the other hand, the bottom sample has a periodic cell length of 40 nm and results in a stable multi-domain structure with two variants. This is possible because the two domains differ by more than just the monoclinic angle. We believe that the domain walls of the 40 nm sample have less mobility, and are able to stabilize the multi-domain structure without the need for applied mechanical constraints.

The other sizes tested, with periodic cell lengths of 4.2 nm, 7 nm, 10nm, and 15nm, all transformed to a single domain of martensite upon cooling. All samples were able to transform back into a single domain of austenite identical to the original configuration upon heating.

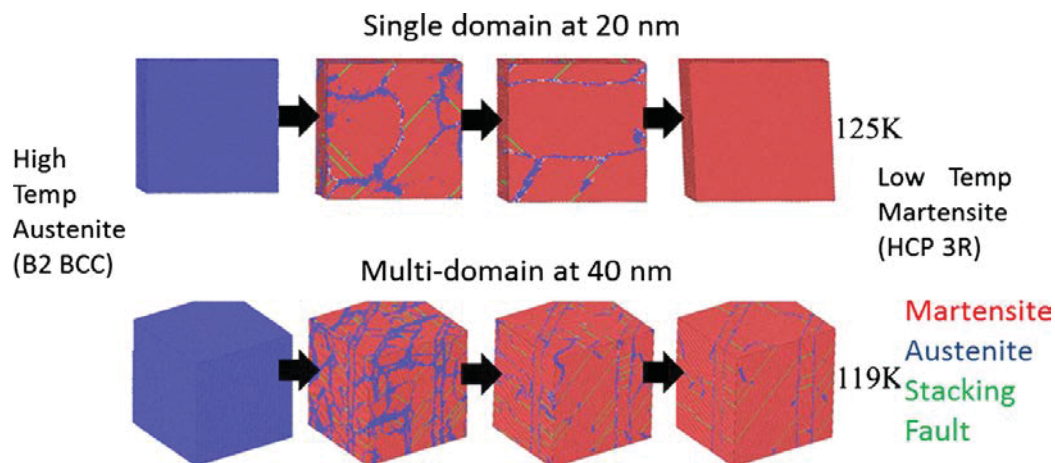


Figure 3.4: Atomistic snapshots from Ovito that illustrate the temporal evolution of the microstructure during the martensitic transformation of $\text{Ni}_{63}\text{Al}_{37}$ disordered SMAs. Red atoms signify martensite (HCP-like), blue atoms represent austenite (BCC-like), and green atoms show stacking faults (FCC-like). The 20 nm structure (top) results in a single domain of martensite upon cooling. The 40 nm structure (bottom) transforms and maintains a two-domain microstructure of martensite upon cooling.

CHAPTER 4. EFFECT OF MECHANICAL CONSTRAINTS ON MARTENSITIC TRANSFORMATION

4.1 Reason for Mechanical Constraints

In practice, most SMAs are polycrystalline materials. Transformation in such materials will result in significant mechanical constraints due to the shape change of the martensitic transformation and the relative orientations of nearby grains. Simulating polycrystalline materials is computationally expensive, so an alternative method was used to impose artificial mechanical constraints on single crystal samples in order to emulate the conditions of a polycrystal. This is achieved by fixing the simulation cell angles at 90° and allowing the cell lengths to still vary independently.

4.2 Transformation Temperatures

The simulations shown in Chapter 3 were repeated with the proposed mechanical constraints. Figure 4.1 shows transformation temperatures as a function of the number of atoms when mechanical constraints are applied by fixing all cell angles to 90° . The transformation temperature to martensite changed little, while the austenite transition temperature showed great size dependence. As system size is decreased from 20 nm to 4.2 nm, the martensitic transformation temperature is approximately halved. This size dependence can be attributed to the ability of martensite to form a multi-domain structure. A larger

system size is able to better accommodate the internal strain caused by the mechanical constraints, resulting in austenite transformation temperatures closer to the unconstrained systems. Smaller sizes are very unhappy and transform back to austenite much more easily.

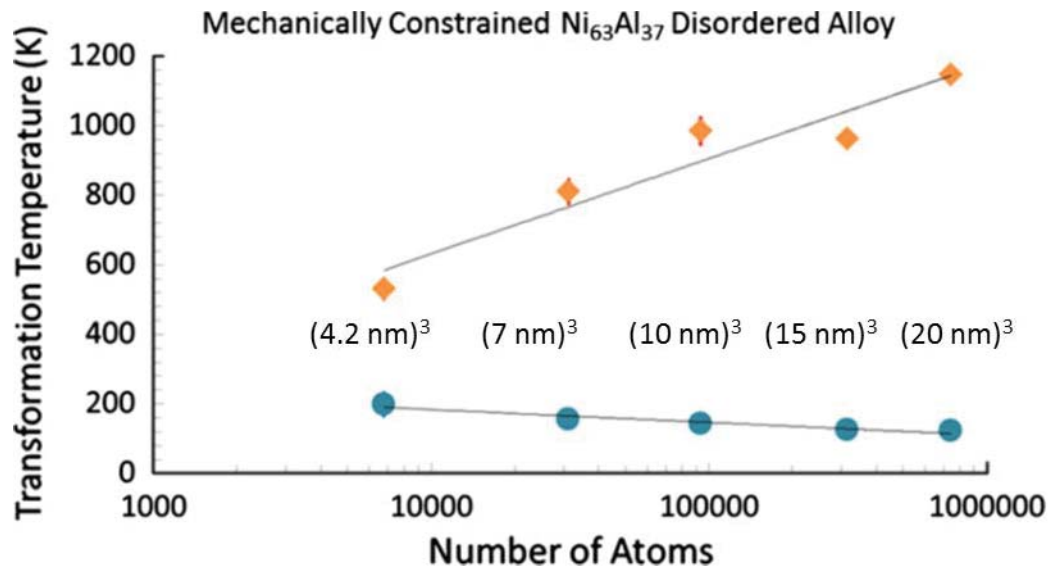


Figure 4.1: The transformation temperatures as a function of system size for $\text{Ni}_{63}\text{Al}_{37}$ SMAs under mechanical constraints. The austenite transition temperature shows strong size dependence and decreases with decreasing size.

Figure 4.2 illustrates the mechanically strained sample-to-sample variability of the transition temperature for all system sizes. The main difference from the unconstrained systems is that the fluctuation of the transformation temperature back to austenite upon heating increases with decreasing system size. This can be accredited to the much lower austenite transformation temperature, which further supports our previous argument that atomic variability between samples affects the relative entropy between austenite and martensite less than it affects the internal energy.

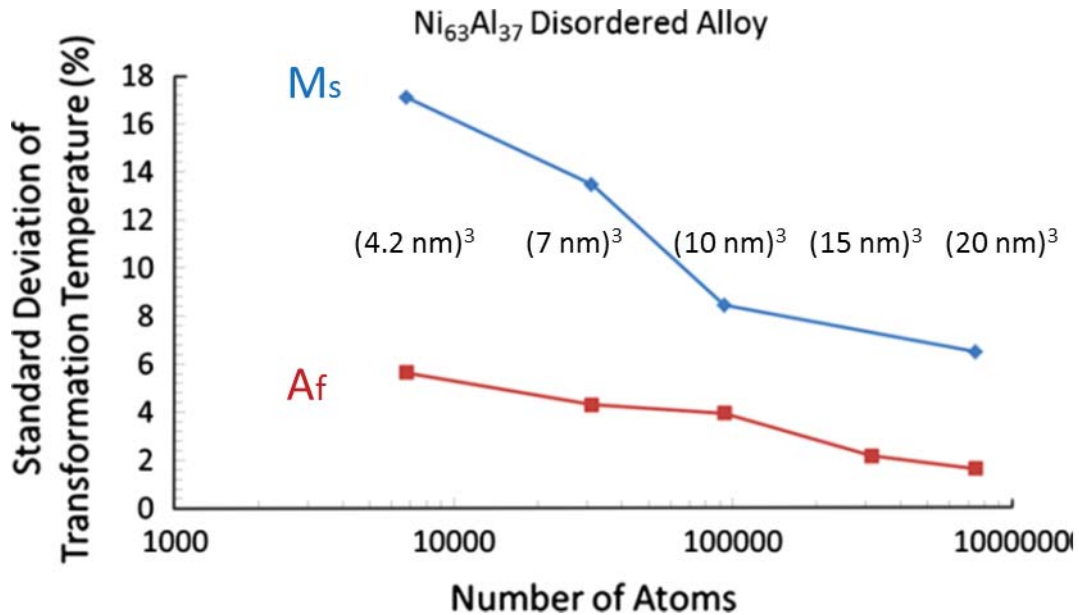


Figure 4.2: The relative fluctuation as a function of system size for Ni₆₃Al₃₇ disordered SMAs under mechanical constraints. Relative fluctuation is defined as the ratio of the standard deviation to the mean. The variability of the transformation back to austenite now increases with decreasing size, due to the mechanical constraints lowering the austenite transformation temperature for smaller system sizes.

4.3 Martensite Microstructure: Role of Mechanical Constraints

Since the transformation results in a change of the lattice parameters and one of the cell angles, it can be expected that fixing all cell angles would result in different martensite structures. Figure 4.3 compares Ovito snapshots between the constrained and unconstrained systems for each system size. Before, we found that the unconstrained systems only formed a multi-domain structure at a periodic cell size of 40 nm, while all other sizes (between 4.2 and 20 nm) resulted in a single domain. For the constrained systems, all sizes exhibited a two-domain structure except for the smallest size with a periodic length of 4.2 nm.

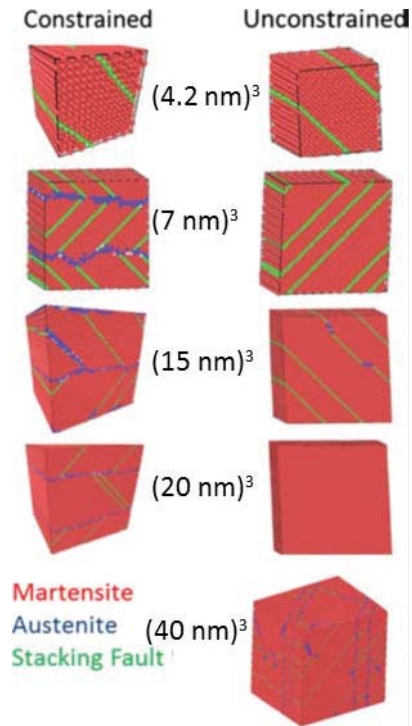


Figure 4.3: Atomistic snapshots from Ovito that compare the martensitic microstructure between the constrained and unconstrained systems. The only unconstrained system that resulted in a multi-domain structure is for $L = 40$ nm. The constrained systems formed a multi-domain structure for periodic cell sizes as small as $L = 7$ nm.

Multi-domain structures are formed in order to reduce the internal stresses. If the system is constrained, the formation of a two-domain structure (as seen in Figure 4.3) allows the structure to release internal stresses and lower its free energy. The two variants are opposite in orientation and equal in size, resulting in the best case scenario for the strain relaxation.

The unconstrained case ($L = 40$ nm) formed a different type of multi-domain structure, with domain walls along the $(110)_{B2}$ plane. The two variants cannot consume one another, resulting in an immobile domain boundary and a stable multi-domain structure. The constrained case does form a multi-domain

structure, but the domain wall is mobile. The artificial constraints keep the two variants from consuming one another by imposing a strain on the system. The system is therefore forced to keep two domains to relax the internal stresses.

CHAPTER 5. MARTENSITIC TRANSFORMATION IN NANOCRYSTALLINE SAMPLES

5.1 Polycrystalline Structures

After analyzing mechanical constraints in single-crystal structures, we switched over to polycrystalline simulations to characterize the transformation in a more realistic setting. In a polycrystalline material, the grains will transform and impede one another, imposing constraints on their neighboring grains. These constraints will affect the transformation temperature and the degree of transformation.

The polycrystalline samples were generated using the Voronoi method. We specify both the simulation cell size and the average grain size. The algorithm produced a structure with a Gaussian distribution of grain sizes centered on the average grain size inputted. The cubic B2 basis of 1 Ni atom and 1 Al atom is replicated in three dimensions to generate each grain, and then we randomly replace Al atoms with Ni atoms until a composition of 63% Ni is obtained. Grain sizes of 2.5, 3.5, 5, 7.5, 10, 15, and 20 nm were investigated.

5.2 Temperature Induced Transformations

The martensitic phase transformation can be induced by either cooling or straining. The temperature induced transformation occurs when the SMA is quenched below the martensitic transformation temperature. All structures were

equilibrated for 200 ps. After equilibration, the samples were cooled from 300K to 1K at a cooling rate of 0.5 K/ps.

Figure 5.1 shows the percent martensite after cooling as a function of grain size. The percentage martensite is calculated by taking the summed percentage of HCP-like and FCC-like atoms, where grain boundary atoms are not considered in the total. As grain size is increased, more of the material transforms into martensite. Interestingly, below a critical grain size of 7.5 nm, the percent transformation increases. We find that the larger, less constrained grains show a large degree of transformation within the grains. The medium sized grains are more constrained and minimal martensite forms close to the grain boundaries. The smallest grains are very constrained, and martensite also forms at the grain boundaries. We believe the smallest grains show an increase in transformation due to rotation of the extremely small grains via grain boundary sliding in order to accommodate elastic strain from the transformation.

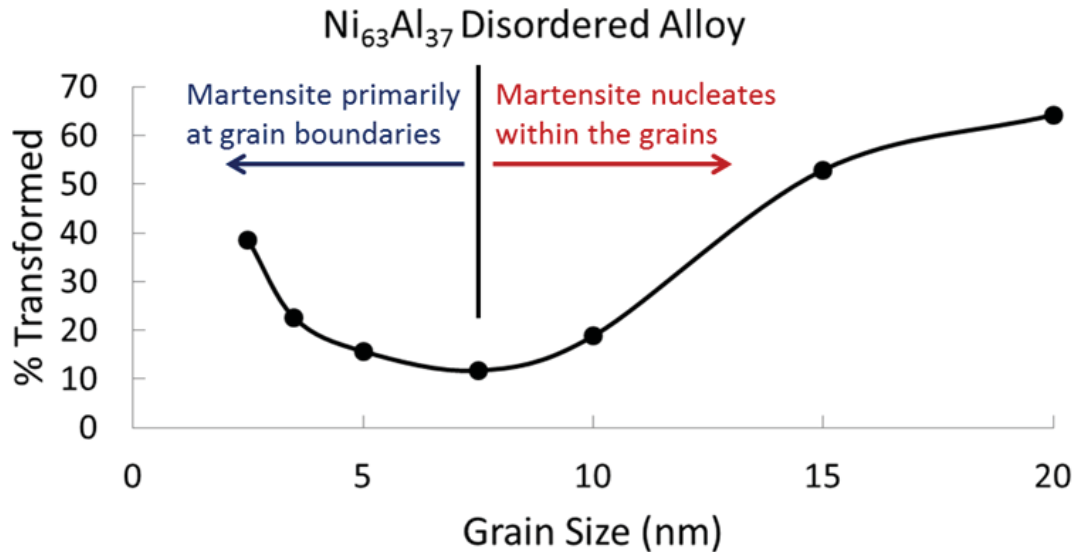


Figure 5.1: Percent martensite transformation vs. grain size for $\text{Ni}_{63}\text{Al}_{37}$ disordered SMAs after cooling to 1K at 0.5 K/ps. Percentage transformation is determined by the summed percentage of HCP-like and FCC-like atoms, where grain boundary atoms are not considered in the total.

Figure 5.2 displays atomistic snapshots of the cooled martensite microstructure for several grain sizes ranging from 3.5 to 20 nm. Again, the blue (BCC-like) atoms represent the high temperature austenite phase, while red (HCP-like) and green (FCC-like) represent the low temperature martensite phase. The 3.5 nm grain size (top left) achieves a martensite transformation of approximately 23%. There are clusters of martensite clinging to the grain boundaries. As grain size is increased, we reach the critical grain size of 7.5 nm (top right), at which there is a minimum in the martensite transformation. The percent transformed only reaches approximately 12% at this grain size, and martensite exists both on grain boundaries and within the grains.

For the grain sizes of 15 nm (bottom left) and 20 nm (bottom right), the transformation primarily occurs within the grains and the martensite domains are

able to grow substantially larger than in the smaller grain sizes. The 15 nm grain size reaches about 53% transformed, while the 20 nm grain size reaches the highest percentage of about 64% transformed.

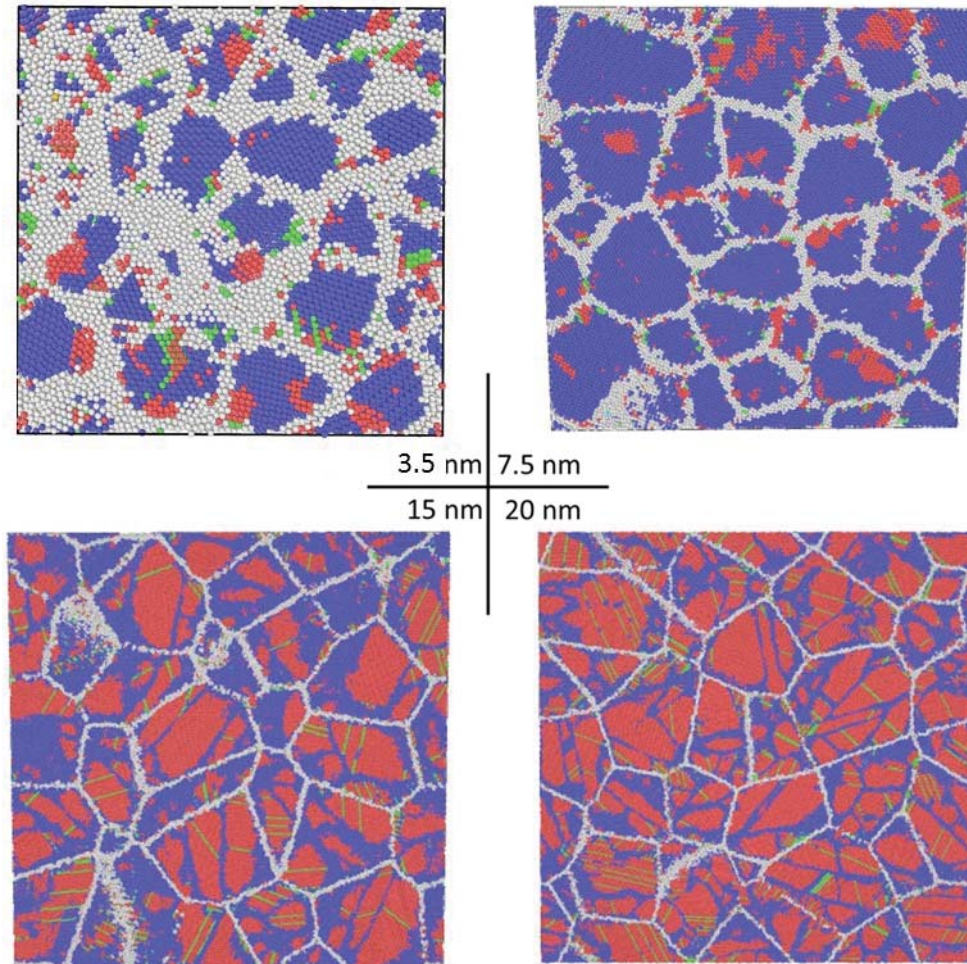


Figure 5.2: Atomistic snapshots of martensite structures after cooling for a range of grain sizes of $\text{Ni}_{63}\text{Al}_{37}$ disordered SMAs. Blue atoms (BCC-like) represent austenite, while red (HCP-like) and green (FCC-like) atoms represent martensite.

Figure 5.3 depicts the percent transformation as a function of temperature during cooling for a range of grain sizes. The largest grain sizes of 15 and 20 nm show an abrupt transformation between about 75 and 125K. These sizes are able to exceed 50% transformation when cooled down to 1K. It is interesting to

note that above the transformation temperature there is less than 5% martensite for these sizes.

On the other hand, the very small grain sizes of 2.5 and 3.5 nm start out with approximately 40% and 20% transformed, respectively. These small sizes show very little transformation during cooling, indicating that most of the transformation occurred at room temperature during the equilibration. This can be explained by the energetically unfavorable atoms at the grain boundaries transforming to martensite in order to relieve stress, as well as possible grain boundary sliding to allow for more transformation.

The middle grain sizes of 7.5 and 10 nm show an increase in slope beginning at around 100K, due to the nucleation and growth of martensite within the grains. This effect is much more noticeable in the aforementioned grain sizes of 15 and 20 nm, where the transformation is much more abrupt and the domains of martensite are able to grow close to their maximum size within the grains. Looking back at Figure 5.2, it is evident that for the grain sizes of 15 and 20 nm, the domains of martensite start to impinge on the grain boundaries as well as one another. For the largest size of 20 nm, the domains of martensite are near fully grown. Several variants exist within a grain, and they grow until they reach a grain boundary or another domain. Interestingly, there exists a small region of austenite (bcc-like atoms) between the variants that acts as a separator. We believe that beyond a grain size of 20 nm the percent transformed will level off, as most of the grains are already saturated with martensite.

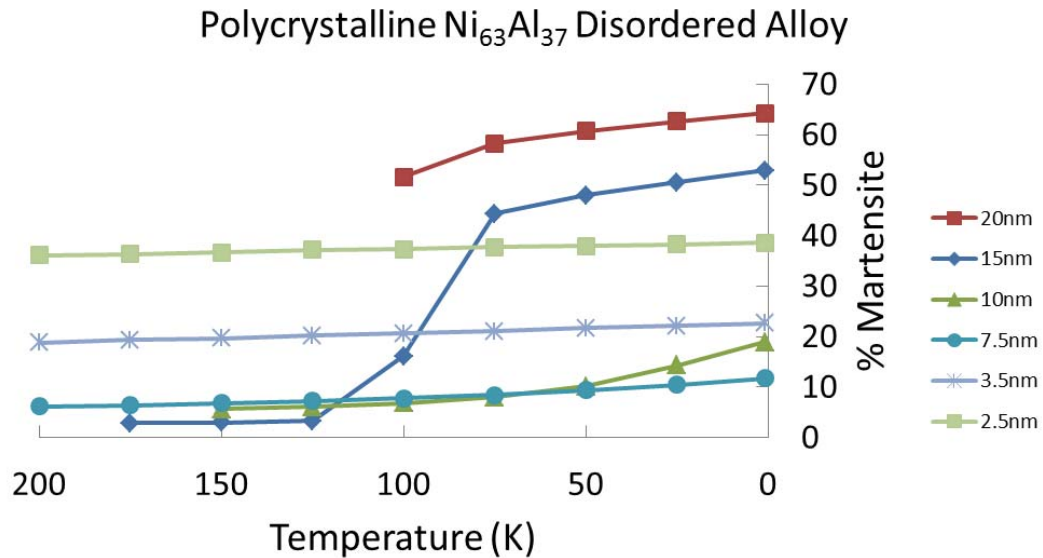


Figure 5.3: Percentage martensite as a function of temperature for different grain sizes of polycrystalline Ni₆₃Al₃₇ disordered SMAs.

5.3 Stress Induced Transformation and Superelasticity

The martensite transformation can also be achieved by applying stress to strain the sample. The transformation from the cubic austenite to the tetragonal martensite involves an expansion along two directions and contraction along the third. By applying a uniaxial stress, the sample can be forced to transform mechanically. The transformation will begin in the favorably oriented grains. The transformed regions will then impose a stress on neighboring grains. Further applied stress will result in additional transformation of martensite. The local strain will determine where and in what orientation the martensite variants will form and grow.

Figure 5.4 shows stress as a function of engineering strain for a range of grain sizes. The samples are strained up to 10% in one direction over 500 ps at

300K. This comes out to a fixed rate of $2 \times 10^8 \text{ s}^{-1}$. The other 2 dimensions were kept at atmospheric pressure. At strains of 4 and 10%, the samples were unloaded and then relaxed to determine recoverability. This was achieved by switching from strain controlled to stress controlled. The stress was reduced to atmospheric pressure over 500 ps at a constant rate, and then the sample was relaxed for an additional 500 ps at atmospheric pressure.

For grain sizes of 10 and 15 nm, a local maximum occurs at a strain of approximately 2 and 1.5 percent, respectively. The peak corresponds to the onset of nucleation of martensite within in grains. The required stress to strain the material lowers as the martensite variants grow. When the martensite begins to be impeded by grain boundaries and other variants, the stress required to strain the material increases. Interestingly, these large grain sizes show a large degree of work hardening. Smaller grain sizes show a more gradual increase in stress and do not have a local maximum of stress. This can be explained by the lack of nucleation and growth of martensite within the grains for smaller grain sizes.

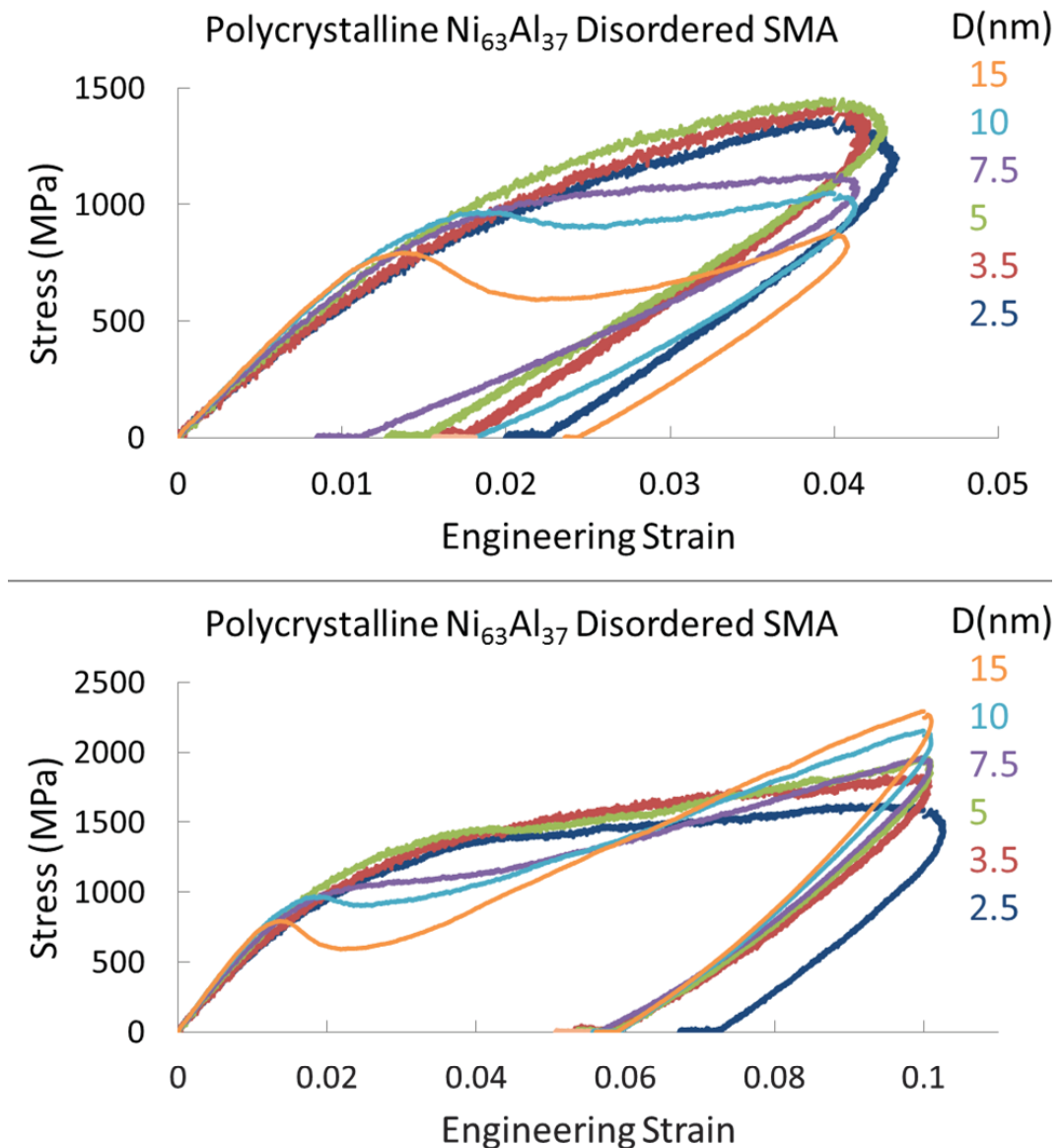


Figure 5.4: Compilation of stress vs. strain curves for a range of grain sizes of $\text{Ni}_{63}\text{Al}_{37}$ disordered SMAs. The samples were strained uniaxially up to 10%. At 4% and 10% strain, the samples were unloaded and relaxed.

Figure 5.5 shows atomistic snapshots of the straining of a polycrystalline sample with a grain size of 3.5 nm. The white grain boundary atoms (classified as other in Ovito) are removed from these snapshots. The left image shows the equilibrated structure, where martensite has already formed at room temperature

at the grain boundaries. The middle image shows the structure held at 10% strain; many grains are fully transformed, while a few show almost no transformation. This supports the idea that favorable grains transform first, and that local stresses can severely hinder transformation in certain regions. The final image on the right shows the strained structure after being relaxed at room temperature. It is clear that some of the transformation was reversed, and that some of the strain was recovered.

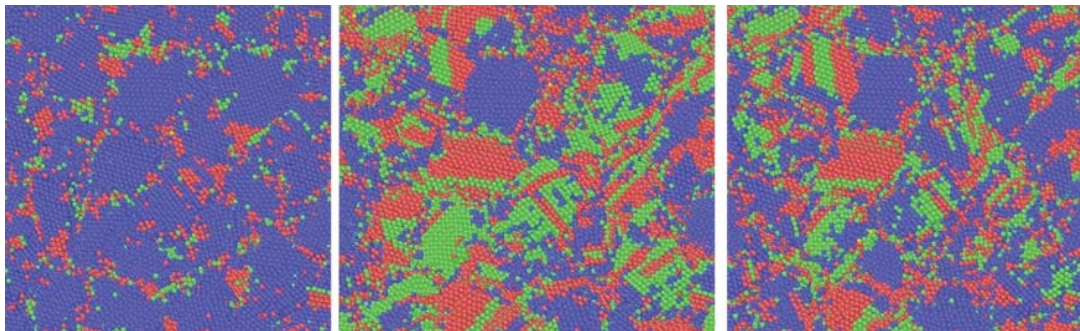


Figure 5.5: Atomistic snapshots of a polycrystalline $\text{Ni}_{63}\text{Al}_{37}$ disordered SMA with a grain size of 3.5 nm. Left-to-right illustrates the microstructure from (1) equilibrated, (2) strained to 10%, and (3) relaxed after 10% strain. Blue atoms are BCC-like, red atoms are HCP-like, and green atoms are FCC-like.

There is great importance in the material's ability to recover from large deformation, also known as superelasticity. Figure 5.6 shows the percent plastic recovery as a function of grain size for strains of 4 and 10%. The plastic recovery was calculated as follows:

$$\text{Plastic Recovery \%} = ((\varepsilon_{\text{plastic}} - \varepsilon_{\text{relaxed}}) / \varepsilon_{\text{relaxed}}) * 100 \quad (5.1)$$

where plastic strain was calculated by:

$$\varepsilon_{\text{plastic}} = \varepsilon_{\text{applied}} - \varepsilon_{\text{elastic}} \quad (5.2)$$

where elastic strain was calculated using:

$$\varepsilon_{elastic} = \frac{\sigma_{applied}}{E} \quad (5.3)$$

Essentially, the elastic part of the strain was subtracted out, and then the percent recovery refers to how much of the plastic part of the strain is recovered. The Young's Modulus was calculated at 0.02% strain, where loading was still very linear.

For the applied strain of 4%, we see a large difference between grain sizes. There is a maximum plastic recovery of over 60% at a grain size of 7.5 nm. The recovery sharply decreases as grain size is either increased or decreased. This can be explained by the graph in Figure 5.1, where we see a minimum degree of transformation at the grain size of 7.5 nm. We believe that since the 7.5 nm grain size structure does not like to transform to martensite much, that it will be more able and willing to reverse the transformation and recover more of the plastic strain upon unloading.

For an applied strain of 10%, we see less plastic recovery and no clear grain size dependence. With the exception of 2.5 nm grain size, all cases show a plastic recovery between 20 and 30 percent.

Three main ideas can be taken from the plot in Figure 5.6. First, the smaller applied strain of 4% resulted in more plastic recovery overall, which is to be expected. Also, the smallest grain size (2.5 nm) shows considerably less plastic recovery than all other grain sizes. Finally, the grain size of 7.5 nm showed the best plastic recovery, especially for smaller strains. This is because of all the grain sizes studied, the grain size of 7.5 nm resulted in the least amount

of transformation to martensite upon cooling; this indicates that the structure favors the austenite phase and is more able to transform back to austenite when the stress is unloaded.

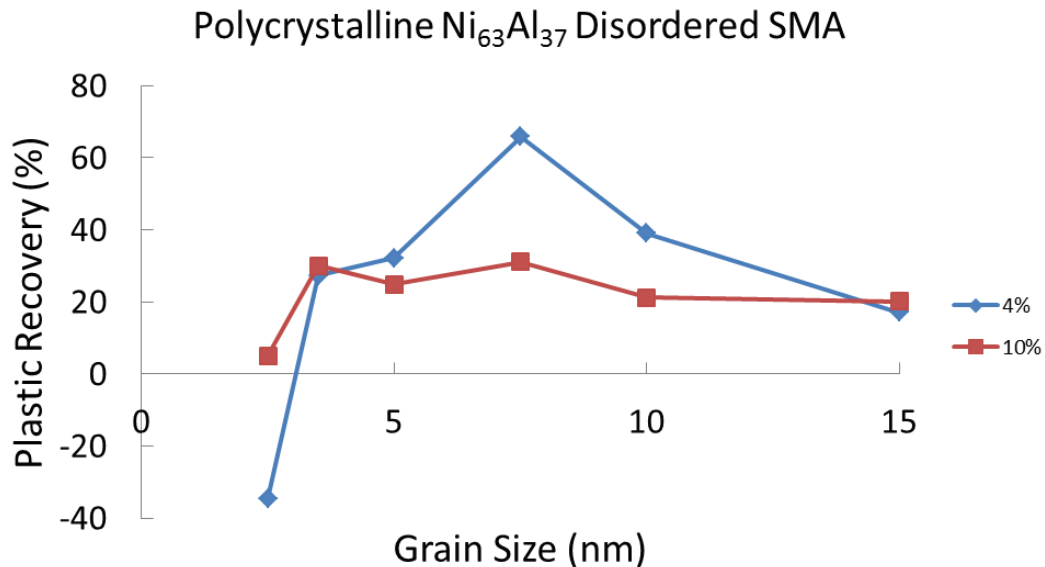


Figure 5.6: Percent plastic recovery as a function of grain size for polycrystalline samples of Ni₆₃Al₃₇ disordered SMAs that were strained to either 4 or 10% and subsequently unloaded and relaxed at room temperature.

Figure 5.7 shows the grain size dependence of Young's Modulus for the different grain sizes. Modulus was calculated using a strain offset of 0.02%, which was very early and corresponds to linear, elastic loading. The Young's Modulus for all grain sizes was approximately 80 GPa. Experiments on equiatomic NiAl show that $E_{\langle 100 \rangle}$ is a soft direction, while $E_{\langle 111 \rangle}$ is much stronger (by a factor of 2.9) at room temperature for a single crystal. From single crystal experiments at room temperature, $E_{\langle 100 \rangle}$ is about 95 GPa, while $E_{\langle 111 \rangle}$ is about 300 GPa [41]. Further MD work could be done to look at the anisotropy of single crystal samples of Ni₆₃Al₃₇ loaded in various crystallographic directions.

Polycrystalline stoichiometric NiAl was measured to have a Young's Modulus of approximately 188 GPa [41]. The reduced Young's Modulus in this work (~80 GPa) may just be due to the compositional difference between 63 and 50% Ni. Further MD work should be done to look at the Young's Modulus of equiatomic NiAl to compare with experiment.

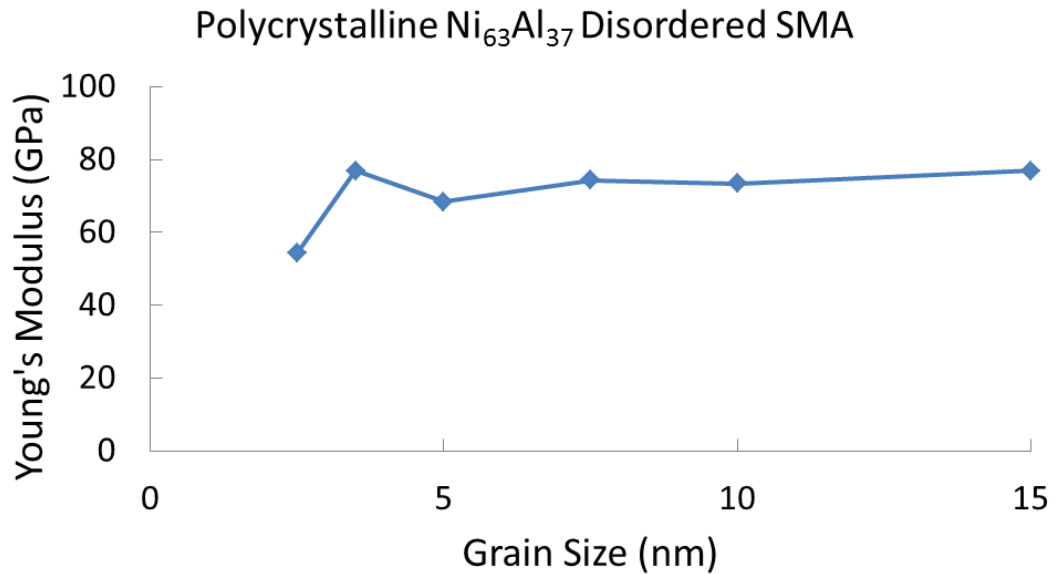


Figure 5.7: Young's Modulus as a function of grain size for polycrystalline samples of Ni₆₃Al₃₇ disordered SMAs.

Plastic strain recovery occurs despite being way below the austenite transition temperature. If we further heat the samples during relaxation, even more of the plastic strain can be recovered. Beyond the austenite transition temperature, full recovery will take place.

CHAPTER 6. CONCLUSIONS AND OUTLOOK

Shape memory alloys are becoming increasingly important as they are being considered for more and more applications. Despite this, much is still not understood about the martensitic phase transformation. The time and spatial resolution needed to directly observe the transformation is unachievable experimentally, as it is a diffusionless process. This is where MD simulation, usually hindered by short time scales, is able to truly shine. Simulations using MD serve as an amazing tool to study the martensitic transformation as it happens, with a timestep as small as one femtosecond. MD simulations using an EAM potential parameterized for NiAl has been successfully employed to study (1) the effects of simulation size on the martensitic transformation, microstructure, and variability, (2) the effects of mechanical constraints on the martensitic transformation and resulting microstructure, and (3) both temperature and stress induced transformation in polycrystalline samples with varying grain size.

MD was used to carry out an extensive set of cooling and heating simulations of $\text{Ni}_{63}\text{Al}_{37}$ disordered SMAs to determine the effect of system size on the martensitic phase transformation and the resulting martensite microstructure. System sizes were studied in the range of 4.2 to 20 nm. We discovered that periodic system size has little effect on the transformation temperature, resulting

in a slight increase with decreasing system size. The variability of the austenite phase transformation between samples resulted in increasing uncertainty with reduced system size. Samples with a periodic cell length of 10 nm showed variability reaching 10% of the mean value of the transformation temperature. On the other hand, the variability of the martensite transformation temperature showed no size effects. This variability can place a fundamental limit on the miniaturization of this class of materials. Future work on surface effects is needed to shed light on how nanoscale samples would behave when reduced to such small sizes.

Mechanical constraints were applied to single-crystal systems using MD simulations in order to understand their role on the transformation in polycrystalline samples of the $\text{Ni}_{63}\text{Al}_{37}$ disordered SMA. All cell angles were forced to remain at 90° . We found that the application of mechanical constraints led to a change in austenite transformation temperature by up to 50%. The mechanical constraints penalize the martensite phase, and led to a very different microstructure. The unconstrained systems all resulted in one domain of martensite, except for the largest case of 40 nm. The applied mechanical constraints favored a multi-domain structure, as the martensite would form two domains to accommodate the internal stresses. All structures resulted in a multi-domain structure, save for the smallest case of 4.2 nm.

Large scale MD simulations were done on polycrystalline samples of the $\text{Ni}_{63}\text{Al}_{37}$ disordered SMA. A range of grain sizes from 2.5 to 20 nm were studied. First, cooling simulations were done to thermally induce the transformation. We

found that a critical grain size of 7.5 nm resulted in a minimum in the percent transformation to martensite. Smaller grain sizes resulted in more transformation at the grain boundaries, possibly due to grain boundary sliding to relieve stress. Larger grain sizes were less constrained and able to nucleate and grow large variants of martensite, resulting in approximately 65% martensite for a grain size of 20 nm. Furthermore, simulations of uniaxial strain were performed to create a stress induced transformation. Larger grain sizes showed considerable work hardening when strained beyond about 2%. The polycrystals were unloaded and relaxed at strains of 4 and 10%. Despite being well below the austenite transformation temperature, the unloading of the stress resulted in considerable recovery of the plastic strain. The samples strained to 10% generally recovered about 20-30% of the plastic strain, while samples strained to 4% recovered varying amounts and peaked with 66% recovery at a grain size of 7.5 nm. If relaxed at higher temperatures, more plastic recovery will occur.

LIST OF REFERENCES

LIST OF REFERENCES

- [1] Duerig T, Pelton A, Stöckel D. An overview of nitinol medical applications. *Mater Sci Eng A* 1999;273-275:149–60.
- [2] Bhattacharya K, James R. The material is the machine. *Science* (80-) 2005;307:53–4.
- [3] Calkins FT, Mabe JH. Shape Memory Alloy Based Morphing Aerostructures. *J Mech Des* 2010;132:111012.
- [4] Ma J, Karaman I. Materials science. Expanding the repertoire of shape memory alloys. *Science* 2010;327:1468–9.
- [5] Otsuka K, Kakeshita T. Science and Technology of Alloys: New Developments. *MRS Bull* 2002:91–100.
- [6] Bhattacharya K, Conti S, Zanzotto G, Zimmer J. Crystal symmetry and the reversibility of martensitic transformations. *Nature* 2004;428:55–9.
- [7] Huang X, Ackland GJ, Rabe KM. Crystal structures and shape-memory behaviour of NiTi. *Nat Mater* 2003;2:307–11.
- [8] Daly S, Ravichandran G, Bhattacharya K. Stress-induced martensitic phase transformation in thin sheets of Nitinol. *Acta Mater* 2007;55:3593–600.
- [9] Kim K, Daly S. Martensite Strain Memory in the Shape Memory Alloy Nickel-Titanium Under Mechanical Cycling. *Exp Mech* 2010;51:641–52.
- [10] Glezer A, Blinova E. Martensite transformation in nanoparticles and nanomaterials. *J Nanoparticle ...* 2003;5:551–60.
- [11] Waitz T, Antretter T, Fischer FD, Simha NK, Karnthaler HP. Size effects on the martensitic phase transformation of NiTi nanograins. *J Mech Phys Solids* 2007;55:419–44.

- [12] Parrinello M, Rahman A. Polymorphic transitions in single crystals: A new molecular dynamics method. *J Appl Phys* 1981;52:7182.
- [13] Meyer R, Entel P. Computer simulations of martensitic transformations in NiAl alloys. *Comput Mater Sci* 1998;10:10–5.
- [14] Shao Y, Clapp P, Rifkin J. Molecular dynamics simulation of martensitic transformations in NiAl. *Metall Mater Trans A* 1996;27:1477–89.
- [15] Thompson A, Strachan A. Complex martensitic nanostructure in Zr nanowires: A molecular dynamics study. *Phys Rev B* 2010;81:085429.
- [16] Sandoval L, Urbassek H. Finite-Size Effects in Fe-Nanowire Solid– Solid Phase Transitions: A Molecular Dynamics Approach. *Nano Lett* 2009;9:2290–4.
- [17] Kastner O, Ackland GJ. Mesoscale kinetics produces martensitic microstructure. *J Mech Phys Solids* 2009;57:109–21.
- [18] Kastner O, Eggeler G, Weiss W, Ackland GJ. Molecular dynamics simulation study of microstructure evolution during cyclic martensitic transformations. *J Mech Phys Solids* 2011;59:1888–908.
- [19] Ackland GJ, Jones a. P, Noble-Eddy R. Molecular dynamics simulations of the martensitic phase transition process. *Mater Sci Eng A* 2008;481-482:11–7.
- [20] Song H, Hoyt JJ. An atomistic simulation study of the migration of an austenite–ferrite interface in pure Fe. *Acta Mater* 2013;61:1189–96.
- [21] Song H, Hoyt JJ. A molecular dynamics simulation study of the velocities, mobility and activation energy of an austenite–ferrite interface in pure Fe. *Acta Mater* 2012;60:4328–35.
- [22] Zhong Y, Zhu T. Patterning of martensitic nanotwins. *Scr Mater* 2012;67:883–6.
- [23] Ni C, Ding H, Jin X. Grain Size Dependence of the Martensitic Transformation in a Nano-grained Fe-Ni Polycrystal—A Molecular Dynamics Study. *J Alloys Compd* 2012;546:1–6.
- [24] Kazanc S, Ozgen S. Thermal and pressure-induced martensitic phase transformations in a Ni–Al alloy modelled by Sutton–Chen embedded atom method. *Mol Simul* 2008;34:251–7.

- [25] Zelazny M, Richardson R, Ackland GJ. Twinning hierarchy, shape memory, and superelasticity demonstrated by molecular dynamics. *Phys Rev B* 2011;84:144113.
- [26] Zhong Y, Gall K, Zhu T. Atomistic characterization of pseudoelasticity and shape memory in NiTi nanopillars. *Acta Mater* 2012;60:6301–11.
- [27] Wang B, Urbassek HM. Molecular dynamics study of the α - γ phase transition in Fe induced by shear deformation. *Acta Mater* 2013;61:5979–87.
- [28] Celik F a., Yildiz a. K, Ozgen S. A molecular dynamics study to investigate the local atomic arrangements during martensitic phase transformations. *Mol Simul* 2011;37:421–9.
- [29] Saitoh K, Liu WK. Molecular dynamics study of surface effect on martensitic cubic-to-tetragonal transformation in Ni–Al alloy. *Comput Mater Sci* 2009;46:531–44.
- [30] Zhang Z, Ding X, Deng J, Cui J. Surface Effects on Structural Phase Transformations in Nanosized Shape Memory Alloys. *J ...* 2013;117:7895–901.
- [31] Kainuma R, Ono N, Ishida K. Development of NiAl (B2)-Base Shape Memory Alloys. *MRS Proc* 1994;360:467–78.
- [32] Lazarev NP, Abromeit C, Schäublin R, Gotthardt R. Temperature-controlled martensitic phase transformations in a model NiAl alloy. *J Appl Phys* 2006;100:063520.
- [33] Plimpton S. Fast Parallel Algorithms for Short-Range Molecular Dynamics 1995;117:1–19.
- [34] Farkas D, Mutasa B, Vailhe C, Ternes K. Interatomic potentials for B2 NiAl and martensitic phases. *Model Simul Mater Sci Eng* 1995;3:201–14.
- [35] Guda Vishnu K, Strachan A. Shape memory metamaterials with tunable thermo-mechanical response via hetero-epitaxial integration: A molecular dynamics study. *J Appl Phys* 2013;113:103503.
- [36] Guda Vishnu K, Strachan A. Shape memory metamaterials with tunable thermo-mechanical response via hetero-epitaxial integration: A molecular dynamics study. *J Appl Phys* 2013;113:103503.

- [37] Guda Vishnu K, Strachan A. Size effects in NiTi from density functional theory calculations. *Phys Rev B* 2012;85:014114.
- [38] Pun GPP, Mishin Y. Molecular dynamics simulation of the martensitic phase transformation in NiAl alloys. *J Phys Condens Matter* 2010;22:395403.
- [39] Lazarev N, Abromeit C, Schäublin R, Gotthardt R. Atomic-scale simulation of martensitic phase transformations in NiAl. *Mater Sci Eng A* 2008;481-482:205–8.
- [40] Stukowski A. Visualization and analysis of atomistic simulation data with OVITO—the Open Visualization Tool. *Model Simul Mater Sci Eng* 2010;18:015012.
- [41] Miracle DB, Darolia R. Chapter 3: NiAl and its Alloys. *Struct. Appl. Intermet. Compd.*, 2000, p. 55–74.

PUBLICATION

PUBLICATION

- Keith R. Morrison, Mathew J. Cherukara, Karthik Guda Vishnu, and Alejandro Strachan. “Role of atomic variability and mechanical constraints on the martensitic phase transformation of a model disordered shape memory alloy via molecular dynamics”. *Acta Materialia* 69, 30-36 (2014).